Interpretation of changes in diffusive and non-diffusive transport in the edge plasma during pedestal buildup following a low-high transition in DIII-D

W. M. Stacey, M.-H. Sayer, J.-P. Floyd, and R. J. Groebner

Citation: Physics of Plasmas (1994-present) **20**, 012509 (2013); doi: 10.1063/1.4775601
View online: http://dx.doi.org/10.1063/1.4775601
View Table of Contents: http://scitation.aip.org/content/aip/journal/pop/20/1?ver=pdfcov
Published by the AIP Publishing

Interpretation of changes in diffusive and non-diffusive transport in the edge plasma during pedestal buildup following a low-high transition in DIII-D

W. M. Stacey,[1,a)] M.-H. Sayer,[1] J.-P. Floyd,[1] and R. J. Groebner[2]
[1]*Georgia Tech, Atlanta, Georgia 30332, USA*
[2]*General Atomics, San Diego, California 92186, USA*

(Received 21 November 2012; accepted 26 December 2012; published online 16 January 2013)

The evolution of diffusive and non-diffusive transport during pedestal buildup following a low-high (L-H) transition has been interpreted from a particle-momentum-energy balance analysis of the measured density, temperature, and rotation velocity profiles in the plasma edge ($0.82 < \rho < 1.0$) of a DIII-D [Luxon, Nucl. Fusion **42**, 614 (2002)] discharge. In the discharge examined, there was an edge-localized-mode-free period of more than 600 ms following the L-H transition, and the majority of edge pedestal development occurred within the first 100 ms following the L-H transition. There appears to be a spatio-temporal correlation among the measured toroidal and poloidal rotation, the formation of a negative well in the measured radial electric field, the creation of a large inward particle pinch, the calculated intrinsic rotation due to ion orbit loss, and the measured formation of steep gradients in density and temperature in the outer region ($\rho > 0.95$) of the edge pedestal. © *2013 American Institute of Physics*. [http://dx.doi.org/10.1063/1.4775601]

I. INTRODUCTION

Soon after the discovery[1] of the high-confinement mode (H-mode) in tokamaks three decades ago, it was realized that the formation of this improved confinement regime was associated with the formation of strong gradients in plasma density and temperature and of a negative well in the radial electric field in the plasma edge (e.g., Ref. 2). Although the H-mode has been actively investigated experimentally in the intervening years (e.g., Ref. 3) and several theories have been put forward for its formation (e.g., Refs. 4–7), the causality of H-mode formation remains an open question and a topic of intense research interest (e.g., Ref. 8 provides a recent summary).

Of particular interest in recent years has been the interpretation of transport processes in the plasma edge from measured profiles of plasma density, temperature, and other variables (e.g., Ref. 9). Systematic procedures for making use of the constraints of particle and energy balance and the thermal conduction relation to infer thermal diffusivities from measurements of temperature and density profiles have been developed (e.g., Ref. 10). More recently, the constraints of particle and momentum balance have been used to develop a methodology for inferring particle diffusion coefficients and non-diffusive particle pinches from measurements of rotation and radial electric field profiles in the plasma edge and for taking into account the effects of non-diffusive ion orbit losses on the interpretation of diffusive and non-diffusive transport from measured profiles.[11,12]

It is the purpose of this paper to apply this particle-momentum-energy-balance-constrained methodology[11,12] to time-resolved measurements of density, temperature and rotation profiles across the pedestal buildup following a low-mode to high-mode (L-H) transition in the DIII-D tokamak.[13] The result is an interpretation of the change in transport parameters from L-mode to H-mode that is required to make the experimental profile measurements satisfy the paradigm of particle, momentum, and energy balance plus the heat conduction relation. Various theoretical models for the physical mechanisms that might actually produce such changes in the transport parameters of this paradigm—the thermal diffusivities and momentum transport frequencies—can then be compared with the interpreted experimental transport parameters, a matter that will be addressed in subsequent investigations.

II. EXPERIMENTAL DATA

In order to examine the evolution of diffusive and non-diffusive transport of the H-mode pedestal following the L-H transition at 1547 ms in a discharge in which there was a long and clear, edge-localized-mode (ELM)-free pedestal buildup to H-mode density and temperature profiles in the plasma edge over ~600 ms. This long ELM-free phase was obtained with a high-triangularity plasma shape (and therefore good magnetohydrodynamic (MHD) stability) and by operating at a heating power that was near the L-H threshold. Fourteen time-slices in this interval were selected for analysis, spanning the late L-mode (1525 ms), early H-mode (1555–1590 ms), transitional pedestal buildup (1640–2040 ms) and fully established pedestal (2090–2140 ms). We have previously compared the L-mode and fully developed pedestal H-mode thermal transport[14] and particle transport[15] properties of this discharge, and have examined the timescale of the pedestal evolution.[16] The purpose of this paper is to extend those investigations to consider the evolution of those properties from the L-mode to fully developed H-mode pedestal, at the same time taking into account advances in the interpretation methodology[11,12] and data analysis procedures.

The electron temperature and density measurements were made with a multipoint Thomson scattering system,[17]

a)Author to whom correspondence should be addressed. Electronic mail: Weston.stacey@nre.gatech.edu

and the carbon temperature, density, and velocity measurements were obtained from measurements of the C VI 5290 line with a charge-exchange recombination (CER) spectroscopy system.[18] A general discussion of such measurements and their errors in DIII-D is given in Ref. 19.

A. Data fitting and analysis procedures

An objective in this work was to obtain the highest time resolution of plasma parameters consistent with accuracy and the characteristics of the data acquisition systems in order to construct the time evolution of plasma property profiles over the L-H transition. The minimum sizes of time bins were selected to contain a sufficient number of Thomson pulses and CER spectroscopy data points to ensure the quality of the data. Experimentally measured quantities include electron density, electron temperature, ion temperature, electron pressure, carbon impurity fraction, carbon toroidal velocity, and carbon poloidal velocity.

It was determined that the optimum balance between quantity and time resolution of data was obtained by requiring that each time bin contain data from a minimum of three pulses each of the CER and Thompson laser systems. This restriction ensured that the data collected would be sufficiently representative of the actual data at each time to provide confidence in the results. The requirement of at least 3 data collection pulses from each system mandated a minimum time width for each bin of around 50 ms. Since the CER system integrating time for data at any one time point is 10 ms, the time interval for the CER pulse associated with a given time was reduced by 5 additional milliseconds on each side to ensure that any points selected fell fully within the designated time interval. After this narrowing, all of the experimental data measurements in a given time bin were collated into a single data set. The bins were selected to extend from just before the L-H transition at 1525 ms to well into H-mode at 2140 ms.

The data fitting procedure involved using a spline-fitted profile to a plot of the composite measured data from the CER system[20] and the use of hyperbolic tangent fits[21] of the data points from the Thomson system for the electron properties. This fitting procedure involved both an automatic profile generation and a manual tuning of the profile through the use of spline knots. After fitting is completed, the ONETWO[22] code is used to calculate the neutral beam effects, the profiles are checked to ensure normalcy and then written to the DIII-D MDSPlus database.

After the profiles had been written to MDSPlus, the GTEDGE[23] input file generation was extracted via specialized scripts that specify variable values at twenty-five rho values. The scripts calculated a large number of quantities at these points, including all of the previously mentioned variables and their gradient scale lengths, as well as time derivatives of several of the variables. These data were then input into the GTEDGE code for analysis. If any suspicious features were found in the profiles of transport variables subsequently calculated by GTEDGE, the fitting procedures for the underlying data were re-examined.

B. Fitted experimental data

The electron density and temperature were measured by Thomson scattering.[17] The fitted experimental electron density and temperature profiles (constructed using the tanh fitting method[21]) shown in Figs. 1 and 2 display a similarity in the evolution of distinct pedestal structures over the pedestal buildup following the L-H transition. Up to about 1640 ms, the location of the edge pedestal position (the point at which the profile changes from a flattop to a steep gradient) changes rapidly, and thereafter continues to change, but more gradually, for both the electron density and temperature profiles. This pedestal position point occurs at a different radius for the density and temperature profiles. (The distance from this point to the separatrix is generally referred to as the "pedestal width.") The electron density and temperature in the flattop region both monotonically increase through the pedestal buildup following the L-H transition.

Experimental ion temperature profiles (measured with CER[18] and fitted using splines[20]) are shown in Fig. 3. The ion temperature profiles, unlike the electron density and temperature profiles, do not develop such a distinctive edge pedestal (separate flattop and sharp gradient regions). A general trend of a monotonic increase in ion temperature over the entire edge region is observed throughout the pedestal buildup following the L-H transition. The major change in ion temperature is observed early in the transition when the ion temperature increases dramatically between 1525 and 1590 ms. The increase in the ion temperature profile is not strictly monotonically, but rather "oscillates" slightly; the peak temperature at the innermost mesh point ($\rho = 0.862$) is achieved at 1940 ms and then decreases slightly by 2140 ms. The ion temperature gradient in the edge pedestal initially increases at the L-H transition and then remains relatively fixed while the entire profile increases.

Measurements of the rotation along tangential and vertical chords were made using CER data,[18] then projected into toroidal and poloidal rotation components. Both rotation velocities were measured for C^{+6} impurity particles. A

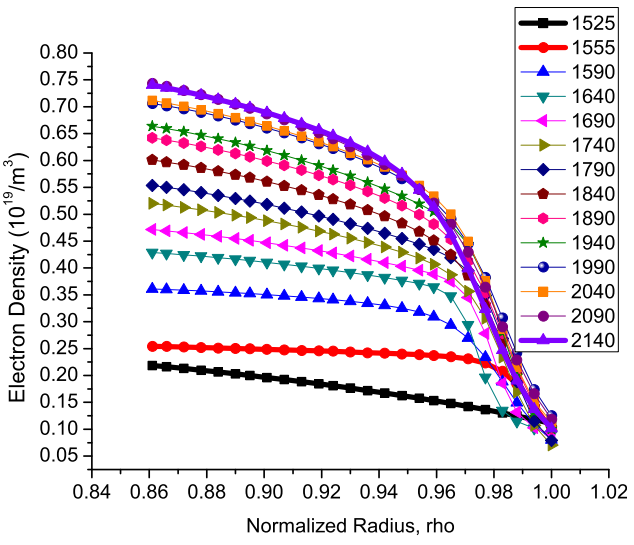

FIG. 1. Fitted experimental electron density profiles.

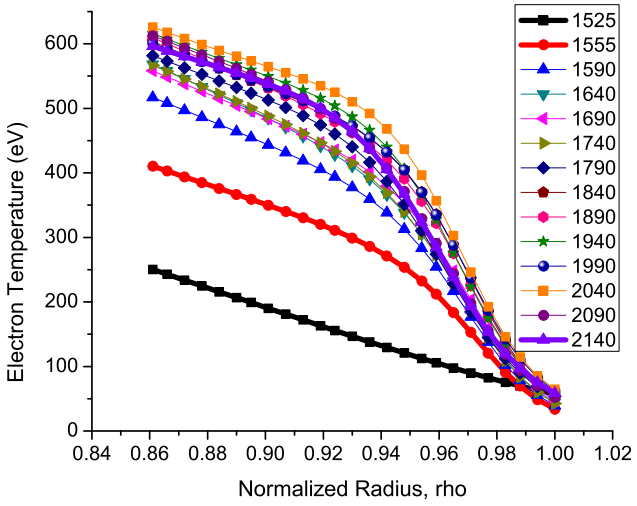

FIG. 2. Fitted experimental electron temperature profiles.

spline fit[20] of the measured toroidal rotation velocity for C^{+6} is shown in Fig. 4.

The toroidal rotation velocity at the innermost radius ($\rho = 0.86$) in the analysis increases steadily as the plasma undergoes the pedestal buildup following the L-H transition. In L-mode (1525 ms), the toroidal rotation profile is relatively flat across the edge region. As the plasma undergoes the L-H transition (1525-1555 ms), a significant change occurs in the toroidal rotation velocity profile. While the rotation velocity increases at the L-H transition for ($\rho < 0.95$), a large region of decreased rotation velocity develops in the edge ($1.0 > \rho > 0.96$). This well-like structure in the toroidal rotation profile persists to about 1740 ms, even though the magnitude of the rotation velocity generally increases at all radii after 1555 ms. Such a radially localized decrease in rotation early in the pedestal buildup following the L-H transition implies either an increased momentum transport rate or a reversed (counter-current) torque, as will be discussed in section II C.

The evolution of the poloidal rotation velocity profiles shown in Fig. 5 displays more distinctive changes than the

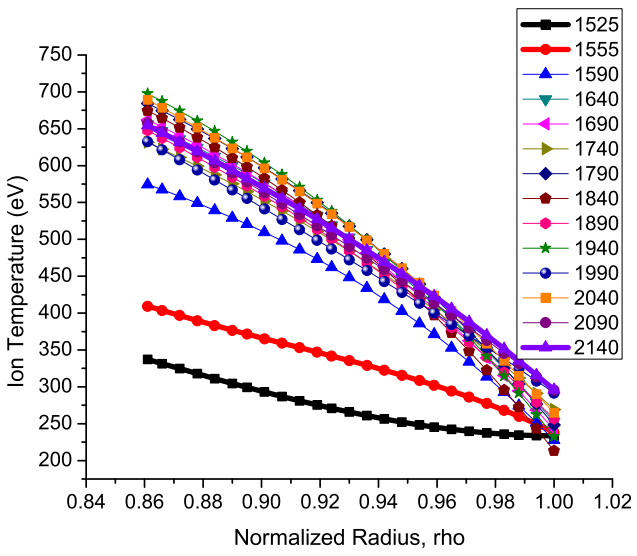

FIG. 3. Experimental ion temperature profiles.

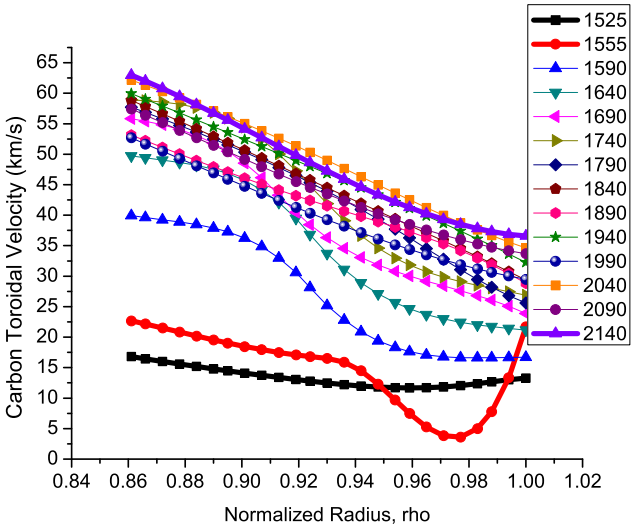

FIG. 4. Carbon toroidal rotation velocity.

toroidal rotation during the pedestal buildup following the L-H transition. In L-mode, the poloidal rotation velocity generally increases with radius, but not monotonically, exhibiting a slight dip centered about $\rho = 0.97$. There is a sharp change in the rotation profile between 1525 ms (L-mode) and 1590 ms (which is not yet complete at 1555 ms) and a continued evolution beyond 1590 ms. The initial evolution changes the direction of the poloidal rotation and creates a broad negative dip centered about $\rho = 0.96$, which persists into the evolving H-mode. The poloidal rotation inside of $\rho = 0.90$ becomes more positive immediately after the L-H transition (1555 ms) but then becomes more negative at later times.

We note that there is possible confusion in the literature about the sign convention of poloidal rotation measurements and reports of agreement or disagreement of measurements with neoclassical theory on different tokamaks. Poloidal rotation is important in this analysis, so this topic is briefly addressed in Appendix, but we note here that since neoclassical poloidal rotation theory is not used in this paper, agreement with neoclassical theory is not an issue for this paper.

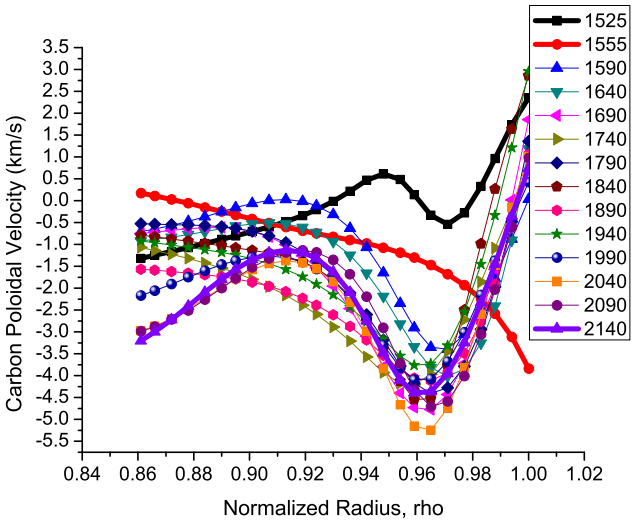

FIG. 5. Carbon poloidal rotation velocity.

C. Inferred (calculated) experimental data

The radial electric field is a calculated quantity constructed from the measured C^{+6} impurity density, temperature, and rotation velocities using the radial force balance equation for carbon ions (indicated by a "k" subscript)

$$E_r = \frac{1}{n_k e_k}\frac{\partial p_k}{\partial r} - (V_{k\theta}\mathrm{B}_\phi - V_{k\phi}B_\theta). \quad (1)$$

The radial electric field profile shown in Fig. 6 evolves in a similar manner to the carbon poloidal rotation velocity profile shown in Fig. 5. In L-mode (1525 ms), the radial electric field profile is relatively flat across the edge region. The profile changes rather quickly after the L-H transition as the plasma pedestal evolves into the H-mode. Early in the evolution (1555 ms), the radial electric field develops a negative well-like structure, as reported in several previous studies (e.g., Ref. 2). This structure is sustained throughout the evolution and into the fully developed H-mode pedestal.

Poloidal and toroidal rotation velocities of deuterium are inferred based on experimental and calculated parameters. The deuterium toroidal rotation velocity is inferred from the measured carbon impurity toroidal rotation velocity, $\mathrm{V}_{\phi k}$, using the carbon and deuterium toroidal momentum balance equations and first order perturbation theory.[24] The perturbation estimate for the difference in toroidal rotation velocities of deuterium and carbon ions is

$$(V_{\phi j} - V_{\phi k})_0 = \frac{(n_j e_j E_\phi^A + e_j B_\theta \Gamma_j + M_{\phi j}) - n_j m_j \nu_{dj} V_{\phi k}^{\exp}}{n_j m_j (\nu_{jk} + \nu_{dj})}, \quad (2)$$

where v_{dj} and v_{dk} are experimental toroidal angular momentum transfer frequencies for deuterium and impurity ions, respectively. Momentum transfer frequencies for deuterium and carbon are calculated as part of the perturbation analysis, based on experimental parameters

$$\nu_{dj} = \frac{(n_j e_j E_\phi^A + e_j B_\theta \Gamma_j + M_{\phi j}) + (n_k e_k E_\phi^A + e_k B_\theta \Gamma_k + M_{\phi k})}{(n_j m_j + n_k m_k) V_{\phi k}^{\exp}}, \quad (3)$$

$$\nu_{dk} = \frac{(n_k e_k E_\phi^A + e_k B_\theta \Gamma_k + M_{\phi k}) + n_j m_j \nu_{jk} (V_{\phi j} - V_{\phi k})_0}{n_k m_k V_{\phi k}^{\exp}}. \quad (4)$$

Using these parameters, the deuterium toroidal rotation velocity shown in Fig. 7 is calculated from

$$V_{\phi j}^{\exp} = V_{\phi k}^{\exp} + (V_{\phi j} - V_{\phi k})_0 = V_{\phi k}^{\exp} + \frac{(n_j e_j E_\phi^A + e_j B_\theta \Gamma_j + M_{\phi j}) - n_j m_j \nu_{dj} V_{\phi k}^{\exp}}{n_j m_j (\nu_{jk} + \nu_{dj})}. \quad (5)$$

The deuterium poloidal rotation velocity is calculated using the deuterium toroidal rotation velocity of Eq. (5) and Fig. 7 in the radial momentum balance equation for deuterium

$$V_{\theta j}^{\exp} = -\frac{E_r^{\exp}}{B_\phi} + \frac{B_\theta}{B_\phi} V_{\phi j}^{\exp} + \frac{1}{n_j e B_\theta}\frac{\partial p_j}{\partial r}. \quad (6)$$

The results are shown in Fig. 8.

The deuterium and impurity ions exhibit similar toroidal rotation velocity profiles. A large negative well-like structure is observed immediately after the L-H transition (1555 ms-1640 ms). Eventually, such structure disappears and relatively linear rotation velocity profiles are observed for both ion species in later stages of the H-mode regime.

For poloidal rotation velocity, very different profile evolutions are observed for the two ion species. For deuterium, a relatively flat rotation velocity profile is inferred in L-mode (1525 ms). This profile quickly changes with the development of a slight dip around $\rho = 0.96$ and a large increase in magnitude of the positive rotation velocity for $\rho > 0.96$. The carbon poloidal rotation velocity of Fig. 5 has a more structured profile in L-mode, and develops a large negative well in the rotation velocity profile for $\rho > 0.96$.

If the deuterium toroidal velocity was measured, as is becoming possible,[25] then the momentum transfer frequencies could be calculated directly from the toroidal momentum balances for the carbon and deuterium ions, and it would not be necessary to use the perturbation theory indicated above. Similarly, if the deuterium poloidal velocity

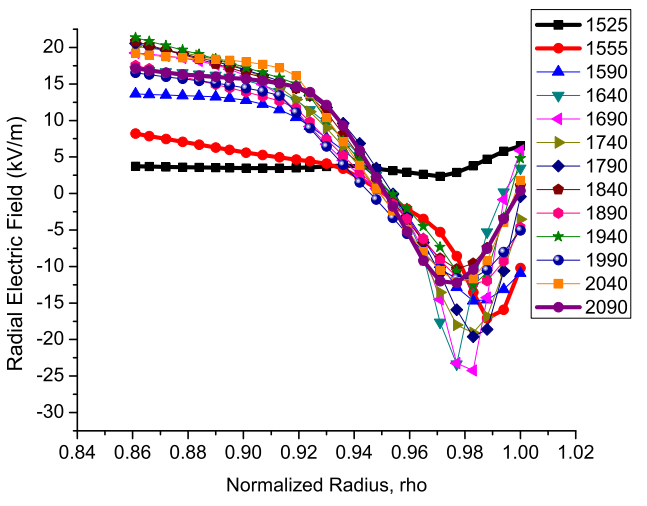

FIG. 6. Radial electric field calculated from radial momentum balance on carbon.

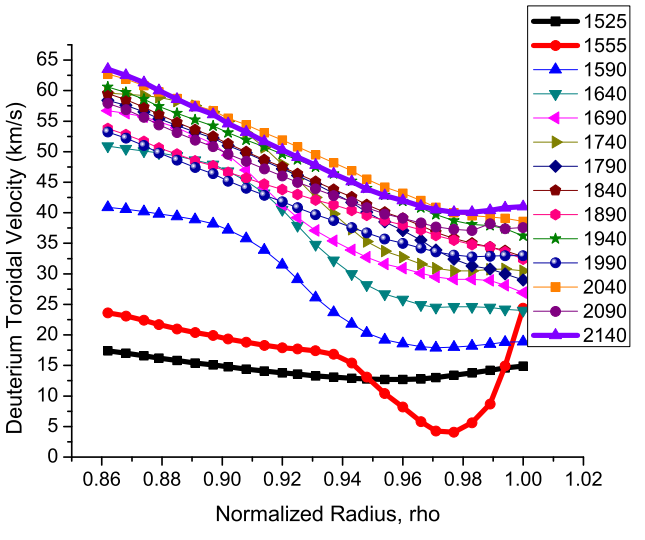

FIG. 7. Calculated deuterium toroidal rotation velocity.

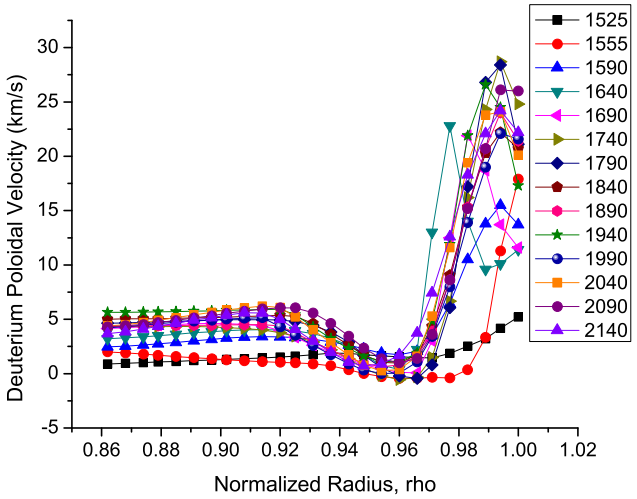

FIG. 8. Calculated deuterium poloidal rotation velocity.

was measured, then it would not be necessary to calculate it from the radial momentum balance, although this would remain a useful confirmation of the consistency of the theory and measurements.

III. TRANSPORT INTERPRETATION OF EXPERIMENTAL DATA

A. Modeling the background plasma with GTEDGE

The background plasma is modeled using the GTEDGE code[23] to supplement the experimental data. GTEDGE solves coupled (i) power and particle balances on the core plasma to obtain particle and power fluxes into the SOL, which are input to (ii) "2-pt" integral power, particle, and momentum balances on the SOL and divertor to calculate power and particle fluxes to the divertor plate and recycling neutral fluxes from the divertor plate, which are input to (iii) a 2D neutral transport calculation of charge-exchange neutral fluxes to the wall and recycling neutral fluxes into the core plasma.

Geometric parameters such as X-pt and divertor strike point locations, plasma minor and major radii and elongation are taken from experiment, as are operating parameters such as the magnetic field and current. The elongated plasma is modeled as a circular plasma with effective minor radius $\hat{r} = r\sqrt{(1+\kappa^2)/2}$ chosen to conserve (in the elliptical approximation) the flux surface area of the elongated plasma with elongation κ.

Other geometric and confinement model parameters and recycling neutral sources are adjusted so that the code predicts experimental (i) line average density; (ii) energy confinement time; (iii) central, edge pedestal and separatrix densities, and temperatures; and (iv) certain other parameters. This GTEDGE background plasma calculation provides the values of particle and heat fluxes crossing the separatrix outward into the SOL and of neutral particle fluxes crossing the separatrix inward to fuel the core plasma, as well as the distribution of neutral particles in the edge plasma.

Using the input experimental density and temperature profile data, the GTEDGE code solves the ion particle continuity equation

$$\frac{\partial(n_j V_{rj})}{\partial r} = -\frac{\partial n_j}{\partial t} + n_e n_o \langle \sigma \upsilon \rangle_{ion} + S_{nb}, \tag{7}$$

for the ion radial particle flux, $\Gamma_j(r) = n_j V_{rj}$, where the second term on the right is the ionization of recycling neutrals and the last term is the neutral beam source. The calculated radial particle flux generally increased with radius in the edge due to the ionization of recycling neutrals, for all times analyzed between 1525 and 2140 ms. The magnitude of the calculated particle flux at all radii increased monotonically in time from 1525 ms (L-mode) until 1940 ms, then decreased monotonically in time until reaching a value about half-way between the 1525 and 1940 magnitudes at 2140 ms.

The GTEDGE code also uses the input experimental density and temperature data to solve the ion and electron power balance equations

$$\frac{\partial Q_j}{\partial r} \equiv \frac{\partial}{\partial r}\left(q_j + \frac{3}{2}\Gamma_j T_j\right) = -\frac{\partial}{\partial t}\left(\frac{3}{2}n_j T_j\right) + q_{nbj} - q_{je} - n_e n_o^c \langle \sigma \upsilon \rangle_{cx} \frac{3}{2}(T_j - T_o^c) \tag{8}$$

and

$$\frac{\partial Q_e}{\partial r} \equiv \frac{\partial}{\partial r}\left(q_e + \frac{3}{2}\Gamma_e T_e\right) = -\frac{\partial}{\partial t}\left(\frac{3}{2}n_e T_e\right) + q_{nbe} + q_{je} - n_e n_k L_k(T_e), \tag{9}$$

for the total heat fluxes of ions and electrons, $Q_i(r)$ and $Q_e(r)$, respectively. The q_{nb} terms represent neutral beam (or other) heating, q_{je} is the ion-to-electron collisional energy transfer, and the last terms in Eqs. (8) and (9) represent charge-exchange cooling of the ions and radiation cooling of the electrons, respectively, which are evaluated using the neutral distribution calculated as part of the background plasma calculation described in the previous paragraph. The quantities $q_{j,e}$ are the conductive heat fluxes of ions and electrons. Similar equations obtain for other ion species "k" present in the plasma, and the electron density is constrained by quasi-neutrality.

The particle and heat fluxes from the GTEDGE background plasma calculation described in the previous paragraph are used as separatrix boundary conditions in solving Eqs. (7)–(9).

The total ion heat flux profile generally decreases with radius at all times considered due to energy exchange with the cooler electrons, with a sharp decrease just inside the separatrix due to charge-exchange cooling from interactions with recycling neutrals. There is initially a monotonic decrease of the ion heat flux profile with time, but after 1590 ms, the change in ion profile with time becomes non-monotonic. The lowest magnitude ion flux profile occurs at 1690 ms and is about half the magnitude of the L-mode profile at 1525 ms, and the magnitude of the profile at the final time analyzed (2140 ms) is about 25% larger than this lowest value.

The total electron heat flux profile generally increases with radius at all times, due to energy exchange with the

hotter ions more than offsetting the radiation losses. The magnitude of the electron heat flux profile exhibits the same variation with time as discussed above for the total ion flux profile, indicating a variation in the total energy flux into the edge region from the core plasma, not a variation in the interaction among ions and electrons in the edge plasma.

Equations (7)–(9) are particle and energy balances which determine the total outward fluxes of particles and energy. For the most part, these fluxes are due to transport processes taking place in the plasma, which we would like to interpret from the measured density, temperature, and rotation profiles. However, some part of these fluxes are in the form of ions which free-stream out of the plasma on loss orbits that intersect with a material surface or cause the ion to be lost by scattering or charge-exchanging outside the last closed flux surface, and the above fluxes need to be reduced by the fraction of the plasma ion particle and energy fluxes due to ion orbit loss.

B. Ion orbit loss

Following Refs. 26 and 27, we make use of the conservation of canonical toroidal angular momentum

$$RmV_{\|}f_{\varphi}+e\psi=const=R_0mV_{\|0}f_{\varphi 0}+e\psi_0, \tag{10}$$

to write the orbit constraint for an ion introduced at a location "0" on flux surface ψ_0 with parallel velocity $V_{\|0}$, where $f_{\varphi}=|B_{\varphi}/B|$, R is the major radius, and ψ is the flux surface value. The conservation of energy and of poloidal angular momentum

$$\begin{aligned}\frac{1}{2}m(V_{\|}^2+V_{\perp}^2)+e\phi=const&=\frac{1}{2}m(V_{\|0}^2+V_{\perp 0}^2)+e\phi_0\\&\equiv\frac{1}{2}mV_0^2+e\phi_0,\\\frac{mV_{\perp}^2}{2B}&=const=\frac{mV_{\perp 0}^2}{2B_0},\end{aligned} \tag{11}$$

further require

$$V_{\|}=\pm V_0\left[1-\left|\frac{B}{B_0}\right|(1-\zeta_0^2)+\frac{2e}{mV_0^2}(\phi-\phi_0)\right]^{\frac{1}{2}}, \tag{12}$$

where ϕ is the electrostatic potential. The quantity $\zeta_0=V_{\|0}/V_0$ is the cosine of the initial guiding center velocity relative to the toroidal magnetic field direction. Using Eq. (12) in Eq. (10) and squaring leads to a quadratic equation in the initial ion speed $V_0=\sqrt{V_{\|0}^2+V_{\perp 0}^2}$

$$\begin{aligned}&V_0^2\left[\left(\left|\frac{B}{B_0}\right|\frac{f_{\varphi 0}}{f_{\varphi}}\zeta_0\right)^2-1+(1-\zeta_0^2)\left|\frac{B}{B_0}\right|\right]\\&+V_0\left[\frac{2e(\psi_o-\psi)}{Rmf_{\varphi}}\left(\left|\frac{B}{B_0}\right|\frac{f_{\varphi 0}}{f_{\varphi}}\zeta_0\right)\right]\\&+\left[\left(\frac{e(\psi_0-\psi)}{Rmf_{\varphi}}\right)^2-\frac{2e(\phi_0-\phi)}{m}\right]=0.\end{aligned} \tag{13}$$

Note that Eq. (13) is quite general with respect to flux surface geometry representation of R, B, and the flux surfaces ψ. By specifying an initial "0" location for an ion with initial direction cosine ζ_0, and specifying a final location on the flux surface ψ, Eq. (13) can be used to determine if an ion with initial speed V_0 and direction cosine ζ_0 can reach that final location on the flux surface ψ.

Thus, Eq. (13) can be solved for the minimum ion energy necessary for an ion located on an internal flux surface to cross the last closed flux surface at a given location or to strike the chamber wall at a given location, etc. All of the ions with speeds greater than this $V_{0\min}(\zeta_0)$ are lost across the last closed flux surface (and assumed in this work not to return) or strike the chamber wall. For the usual DIII-D anti-parallel current/magnetic field configuration, the quantity $V_{0\min}(\zeta_0)$ is very large for particles with parallel velocity components opposite to the direction of the toroidal magnetic field ($\zeta_0<0$), which execute banana orbits inside the flux surface, but becomes smaller with increasing $\zeta_0>0$ (i.e., as the particle velocity becomes more nearly aligned with the toroidal magnetic field direction).

GTEDGE calculates $V_{0\min}(\zeta_0)$, using the electrostatic potential calculated by integrating the input experimental radial electric field, an approximate representation of the magnetic flux surface geometry described by $[R(r,\theta)=\bar{R}h(r,\theta)$, $B_{\theta,\varphi}(r,\theta)=\bar{B}_{\theta,\varphi}/h(r,\theta)$, $h(r,\theta)=(1+(r/\bar{R})\cos\theta)]$, and an approximate flux surface representation $\psi(\rho)=RA_{\varphi}=\frac{1}{2}\left(\frac{\mu_0 I}{2\pi a^2}\right)\bar{R}\bar{a}^2\rho^2$ which follows from Ampere's law and the assumption of uniform current density.

Since $V_{0\min}(\zeta_0)$ decreases with radius, cumulative (with increasing radius) particle, momentum and energy loss fractions can be defined

$$\begin{aligned}F_{orb}\equiv\frac{N_{loss}}{N_{tot}}&=\frac{\int_{-1}^{1}\left[\int_{V_{0\min(\zeta_0)}}^{\infty}V_0^2f(V_0)dV_0\right]d\zeta_0}{2\int_0^{\infty}V_0^2f(V_0)dV_0}\\&=\frac{\int_{-1}^{1}\Gamma\left(\frac{3}{2},\varepsilon_{\min(\zeta_0)}\right)d\zeta_0}{2\Gamma\left(\frac{3}{2}\right)},\end{aligned} \tag{14}$$

$$\begin{aligned}M_{orb}\equiv\frac{M_{loss}}{M_{tot}}&=\frac{\int_{-1}^{1}\left[\int_{V_{0\min(\zeta_0)}}^{\infty}(mV_0\zeta_0)V_0^2f(V_0)dV_0\right]d\zeta_0}{2\int_0^{\infty}(mV_0)V_0^2f(V_0)dV_0}\\&=\frac{\int_{\zeta_0}^{1}\Gamma\left(2,\varepsilon_{\min(\zeta_0)}\right)d\zeta_0}{2\Gamma(2)},\end{aligned} \tag{15}$$

and

$$E_{orb} \equiv \frac{E_{loss}}{E_{total}} = \frac{\int_{-1}^{1}\left[\int_{V_{0min}(\zeta_0)}^{\infty}\left(\frac{1}{2}mV_0^2\right)V_0^2 f(V_0)dV_0\right]d\zeta_0}{\int_{-1}^{1}\left[\int_{0}^{\infty}\left(\frac{1}{2}mV_0^2\right)V_0^2 f(V_0)dV_0\right]d\zeta_0}$$
$$= \frac{\int_{-1}^{1}\Gamma\left(\frac{5}{2},\varepsilon_{\min(\zeta_0)}\right)d\zeta_0}{2\Gamma\left(\frac{5}{2}\right)}, \quad (16)$$

where $\varepsilon_{\min}(\zeta_0) = mV_{0\min}^2(\zeta_0)/2kT$ is the reduced energy corresponding to the minimum velocity for which ion orbit loss is possible, and an initially Maxwellian ion distribution has been assumed. The quantities $\Gamma(n)$ and $\Gamma(n,x)$ in Eqs. (14)–(16) are the gamma function and incomplete gamma function. The ion-orbit-loss-corrected ion particle and energy transport fluxes are then $\widehat{\Gamma}_j(r) = \Gamma_j(r)(1 - F_{orb}(r)), \widehat{Q}_j(r) = Q_j(r)(1 - F_{orb}(r))$.

The particle and energy ion loss fractions given by Eqs. (14) and (16) are shown in Figs. 9 and 10. The ion orbit loss fractions from inner flux surfaces increase after the L-H transition (>1525 ms) because the increase in ion temperature enables a larger fraction of the ion distribution to access loss orbits. The effect of these ion orbit loss fractions in reducing the fluxes that should be used in the interpretation of diffusive transport processes is largest just inside the separatrix, where it significantly reduces the $\hat{\Gamma}_j$ and $\hat{Q}_j$ relative to Γ_j and Q_j, respectively.

C. Intrinsic rotation

The effect of ion orbit momentum loss is somewhat different than for particle and energy loss. In the anti-parallel current/toroidal field configuration of discharge #118897, the usual (but not always) preferential loss of $\zeta_0 > 0$ (counter-current) ions causes a residual $\zeta_0 < 0$(co-current) intrinsic rotation in the edge plasma due to the preferential retention of co-current direction ions. The net co-current rotation velocity at any flux surface is determined by the cumulative net counter-current directed ion orbit loss that has taken place

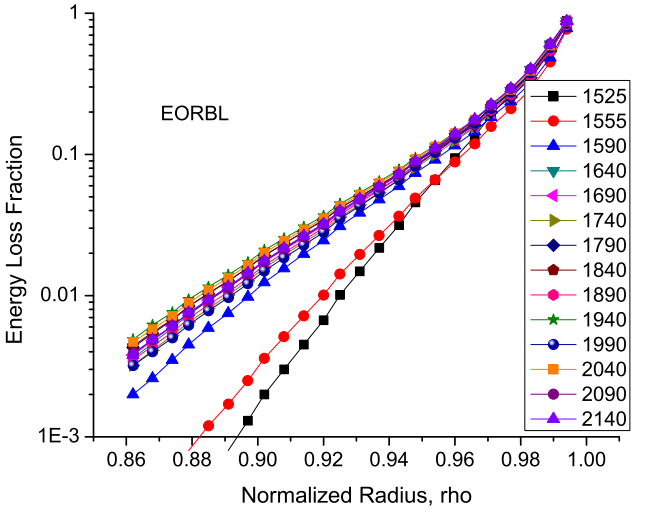

FIG. 10. Energy ion orbit loss fractions.

over all inner radii out to that flux surface in question. Determining the minimum loss speed $V_{\min(\zeta_0)}$ as described above leads to an expression for the net parallel momentum loss (when multiplied by nm)

$$\Delta V_{\parallel}(\rho) = 2\pi\int_{-1}^{1}d\zeta_0\left[\int_{V_{\min}(\zeta_0)}^{\infty}(V_0\zeta_0)V_0^2 f(V_0)dV_0\right]_{\rho}$$
$$= 4\pi M_{orb}(\rho)\left[\int_{0}^{\infty}(V_0)V_0^2 f(V_0)dV_0\right]_{\rho},$$
$$= 2\frac{\Gamma(2)}{\pi^{1/2}}M_{orb}(\rho)V_{th}(\rho) = \frac{2}{\pi^{1/2}}M_{orb}(\rho)\sqrt{\frac{2kT_{ion}(\rho)}{m}}, \quad (17)$$

where M_{orb} is given by Eq. (15). The intrinsic co-current rotation (minus the right side of Eq. (17)) is plotted in Fig. 11 for several times in the evolution of the L-H transition. The intrinsic co-current deuterium rotation in L-mode (1525 ms) increases immediately (1555 ms) after the L-H

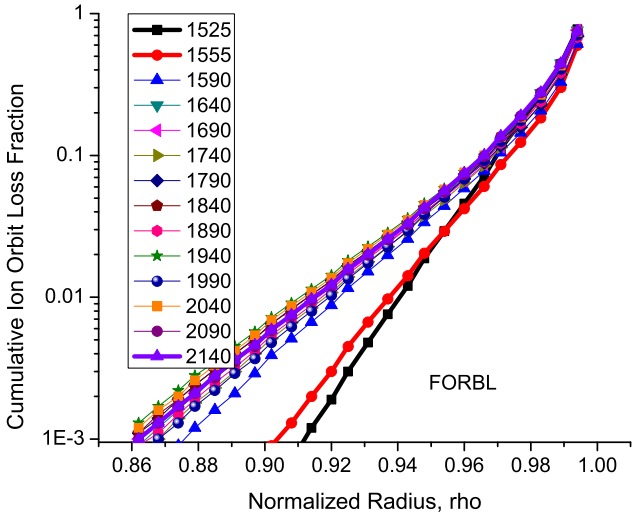

FIG. 9. Particle ion orbit loss fractions.

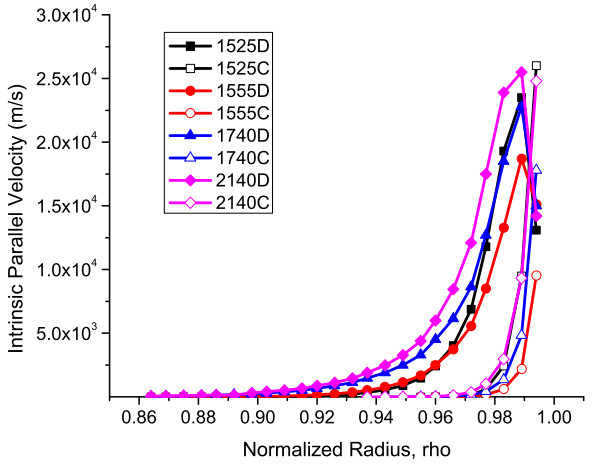

FIG. 11. Intrinsic co-current rotation due to ion orbit loss for deuterium and carbon ions.

transition for $\rho < 0.95$, but decreases for $\rho > 0.95$, which is qualitatively and quantitatively consistent with the increase of toroidal rotation observed for $\rho < 0.95$ and the decrease observed for $\rho > 0.95$ between 1525 and 1555 ms in Fig. 4. This observation suggests that the change in intrinsic rotation due to ion orbit loss between 1525 and 1555 ms may be responsible for the difference in toroidal rotation profiles between 1525 and 1555 ms. This intrinsic co-current momentum constitutes a positive torque $M_\phi^{iol} = nm\Delta V_\parallel$, that if taken into account in interpreting the momentum transport frequencies from Eqs. (3) and (4) would result in even larger values, but this has not been taken into account in the following interpretation of momentum transport frequencies and diffusion coefficients. Intrinsic rotation is discussed in greater detail in Refs. 28 and 29.

D. Interpretation of particle transport

Particle transport is determined by momentum balance. The toroidal and radial components of the second velocity moment, or momentum balance, equation may be written for any ion species "j"

$$n_j m_j[(\nu_{jk}+\nu_{dj})V_{\phi j}-\nu_{jk}V_{\phi k}]=n_j e_j E_\phi^A+n_j e_j B_\theta V_{rj}+M_{\phi j} \quad (18)$$

and

$$V_{\phi j}=\frac{1}{B_\theta}\left[E_r+V_{\theta j}B_\phi-\frac{1}{n_j e_j}\frac{\partial p_j}{\partial r}\right], \quad (19)$$

where "k" in general refers to a sum over other ion species. In this paper, "j" will refer to the main ion (deuterium), and "k" to the impurity ion (carbon) in a two-species model.

The quantity ν_{dj} is a toroidal angular momentum transfer frequency which represents the combined effect of viscosity, inertia, atomic physics, and other "anomalous" processes. Justification for representing the toroidal momentum transfer processes in this form is discussed in Ref. 30. $M_{\phi j}$ is the toroidal momentum input, e_j refers to the charge of species "j", and the other symbols have their usual meaning.

Subject to the assumption that there is a single impurity species "k" with the same logarithmic derivative and the same local temperature as the main ions "j," Eqs. (18) and (19) can be combined to arrive at a constraint on the main ion pressure gradient

$$-\frac{1}{p_j}\frac{\partial p_j}{\partial r}=\frac{V_{rj}-V_{rj}^{pinch}}{D_j}, \quad (20)$$

where the "diffusion coefficient" is

$$D_j \equiv \frac{m_j T_j \nu_{jk}}{(e_j B_\theta)^2}\left(1+\frac{\nu_{dj}}{\nu_{jk}}-\frac{e_j}{e_k}\right) \quad (21)$$

and the "pinch velocity"

$$V_{rj}^{pinch} \equiv \frac{[-M_{\phi j}-n_j e_j E_\phi^A+n_j m_j(\nu_{jk}+\nu_{dj})(f_p^{-1}V_{\theta j}+E_r/B_\theta)-n_j m_j \nu_j V_{\theta k}]}{n_j e_j B_\phi} \quad (22)$$

is a collection of normalized forces associated with the electric field, VxB is the forces and beam momentum input and $f_p = \beta_\theta/\beta_\phi$.

The fundamental transport coefficients that determine the main ion diffusion coefficient are the momentum exchange frequencies with impurities (ν_{jk}) and with neutrals (ν_{cx}), and the momentum transport frequencies across flux surfaces due to viscosity and inertia, and to any anomalous momentum exchange processes (all except ν_{jk} are included in ν_{dj}).

If both the deuterium and carbon toroidal rotation velocities were measured, as is becoming possible,[25] then Eqs. (18) for deuterium and carbon could just be solved for ν_{dj} and ν_{dk}, using the measured velocities as input. In the more common situation where only the carbon toroidal velocity is measured, it is necessary to resort to a perturbation analysis of Eqs. (18) for deuterium and carbon, which leads to Eqs. (2)–(4).

The momentum balance requirement of Eq. (20) can be rearranged into a form that clearly exhibits the diffusive and the non-diffusive components of the radial particle flux

$$\widehat{\Gamma}_j \equiv n_j V_{rj} = -\frac{n_j D_j}{p_j}\frac{\partial p_j}{\partial r}+n_j V_{rj}^{pinch} = -D_j\frac{\partial n_j}{\partial r}-D_j\frac{n_j}{T_j}\frac{\partial T_j}{\partial r}+n_j V_{rj}^{pinch}. \quad (23)$$

The more general case when the assumption made above about the impurity distribution is not made is treated in Ref. 30.

The ion-impurity collision frequencies evaluated using the experimental densities and temperatures, the inferred experimental momentum transfer frequencies of Eq. (3) for deuterium, and the resulting deuterium diffusion coefficient of Eq. (21) are displayed in Figs. 12–14.

The abrupt increase in momentum transport frequency for $\rho > 0.95$ for the 1555 ms time is produced by the measured reduction in toroidal rotation in this region at that time, as shown in Fig. 4. As discussed above, this reduction in toroidal rotation seems, in turn, to be associated with the change in intrinsic rotation produced by ion orbit loss, as shown in Fig. 11. This peaking in the inferred momentum

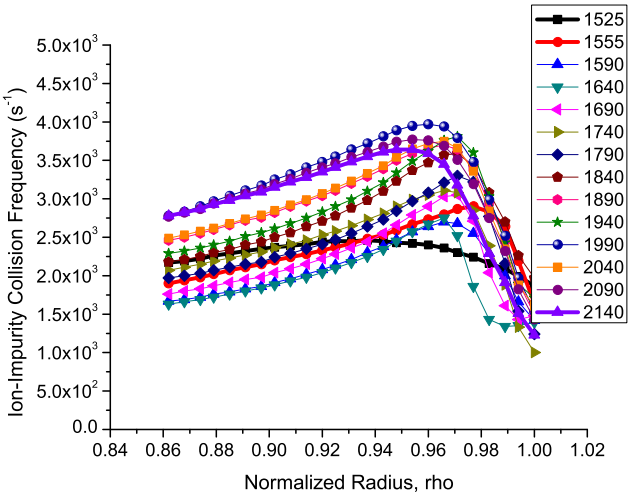

FIG. 12. Ion-Impurity collision frequencies.

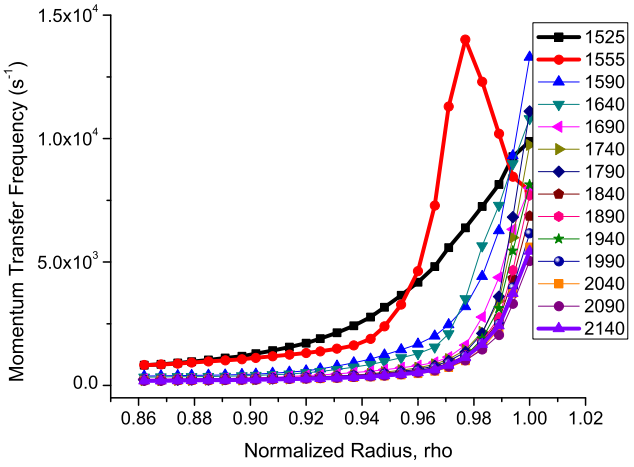

FIG. 13. Toroidal momentum transfer frequencies.

transport frequency is directly reflected as a peak in the diffusion coefficient, as shown in Fig. 14. If, indeed, the peak in the toroidal velocity for $\rho > 0.95$ is due to intrinsic rotation, then it might be more physical to represent the orbit-loss effect as a torque (i.e., include it with the neutral beam torque in the $M_{\phi j}$ term) or to reduce the measured rotation by this intrinsic rotation before inferring the momentum transport frequency and diffusion coefficient.

The pinch velocity of Eq. (22) is slightly outward in L-mode, except just inside the separatrix, but a strongly inward pinch velocity develops over the region $\rho \geq 0.97$ immediately after the L-H transition (between 1525 and 1555 ms), as shown in Fig. 15. The various components of the pinch velocity expression of Eq. (21) are plotted separately in Fig. 16. In L-mode (1525 ms), the E_r and V_θ components are oppositely directed and almost cancel, leaving a small pinch velocity. Immediately after the L-H transition (1555 ms) the E_r component becomes strongly inward, reflecting the strong negative value of the radial electric field just after the L-H transition, and these two dominant components reinforce each other to produce a strongly inward pinch velocity. At later times, the E_r and V_θ components become less strongly inward, as does the net pinch velocity.

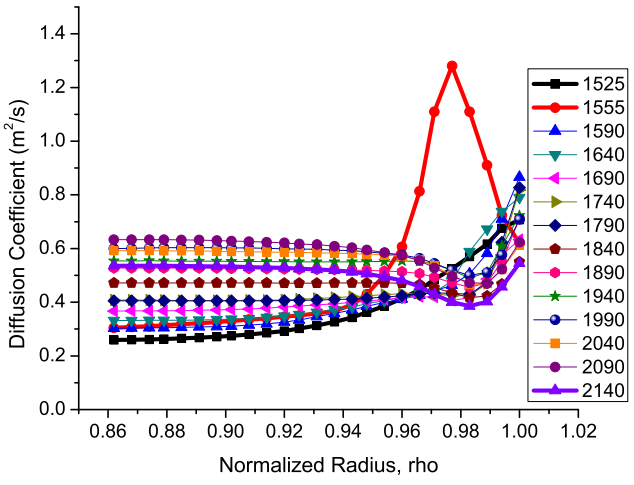

FIG. 14. Deuterium diffusion coefficients.

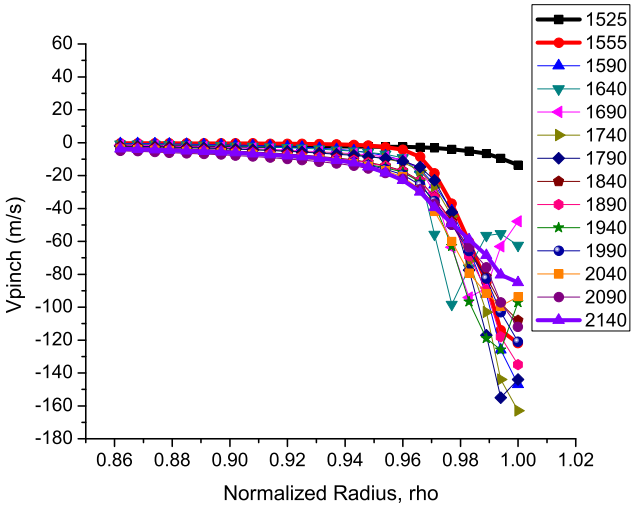

FIG. 15. Pinch velocity.

E. Interpretation of thermal transport

The heat conduction relation

$$q_{j,e} = -n_{j,e}\chi_{j,e}\frac{\partial T_{j,e}}{\partial r} \tag{24}$$

is used to determine the thermal diffusivity from the experimental temperature profiles

$$\chi_{j,e}^{\exp} = -\frac{q_{j,e}^{\exp}}{n_{j,e}^{\exp}(\partial T_{j,e}^{\exp}/\partial r)} = -\frac{(Q_{j,e}^{\exp} - 1.5\Gamma_{j,e}^{\exp}T_{j,e}^{\exp})}{n_{j,e}^{\exp}(\partial T_{j,e}^{\exp}/\partial r)}, \tag{25}$$

where $Q_{j,e}^{\exp}$ is obtained by solving Eq. (8) or Eq. (9) for the total heat flux (and correcting for ion orbit loss for the ions), and $\Gamma_j^{\exp}$ is obtained by solving Eq. (7) for the total radial particle flux (and correcting for ion orbit loss) and $\Gamma_e^{\exp}$ is constructed therefrom taking into account impurities.

The electron thermal diffusivity plotted in Fig. 17 decreases immediately after the L-H transition (between 1525 and 1555 ms) and generally continues to decrease as the H-mode pedestal evolves, forming a "well" or "transport barrier" that moves inward with time following the L-H transition between 1525 and 1555 ms.

The ion thermal diffusivity also decreases at the L-H transition and continues to decrease as the H-mode pedestal evolves, as shown in Fig. 18, but does not seem to form the "well" or "transport barrier" structure seen for the electron thermal diffusivity. The strong effect upon the interpreted ion thermal diffusivity just inside the separatrix of the ion orbit loss correction can be seen by comparing Figs. 18 and 19.

IV. SUMMARY

The evolution of diffusive and non-diffusive transport during a pedestal buildup following the L-H transition has been interpreted from a particle-momentum-energy balance analysis of the measured density, temperature, and rotation velocities in the plasma edge $(0.86 < \rho < 1.0)$ of a DIII-D discharge.

The measured density, temperature, and rotation velocities in the plasma edge and the radial electric field

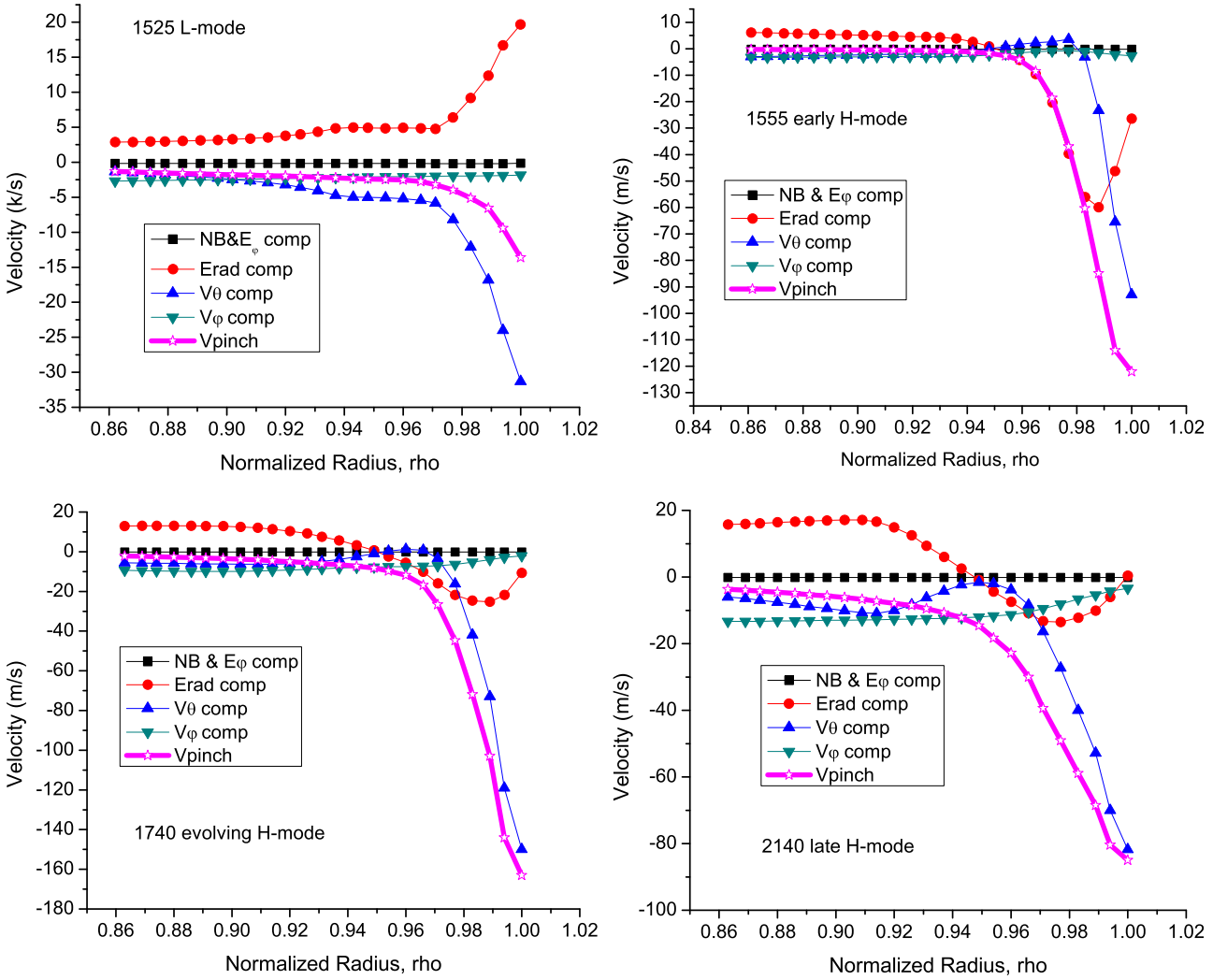

FIG. 16. Components of the pinch velocity at different times.

constructed from them changed dramatically from their L-mode profiles during the first 30–70 ms after the L-H transition and then slowly evolved over another few hundred ms, non-monotonically, as the H-mode pedestal fully developed for about 600 ms before the onset of ELMs. These data and calculated radial heat and particle fluxes were used in the heat conduction relation to interpret experimental thermal diffusivities, and these data were used with the particle and

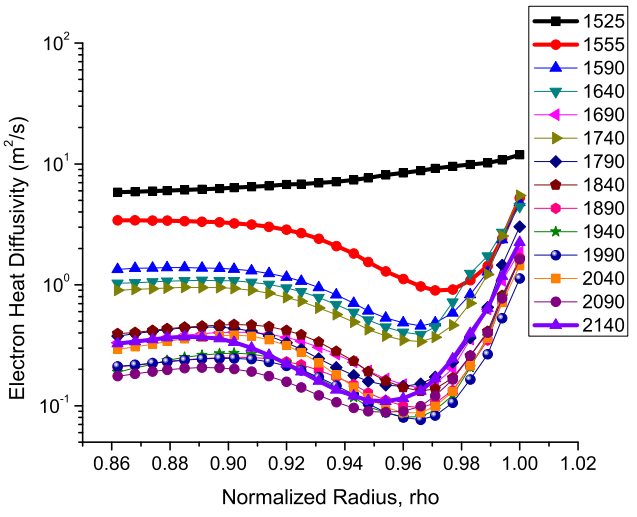

FIG. 17. Experimental electron thermal diffusivity.

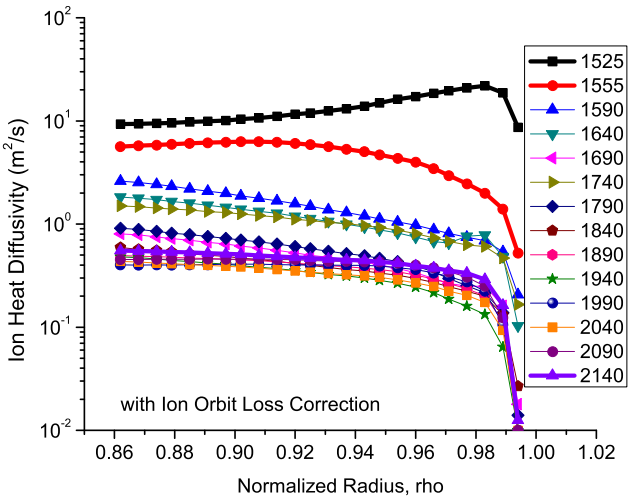

FIG. 18. Experimental ion thermal diffusivity with ion orbit loss correction.

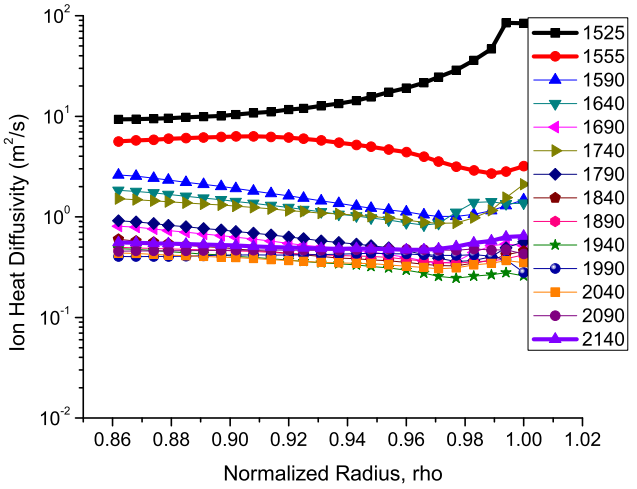

FIG. 19. Experimental ion thermal diffusivity without ion orbit loss correction.

momentum balance equations to interpret experimental particle diffusion coefficients and pinch velocities.

Momentum balance requires that the radial particle flux satisfies a "pinch-diffusion" relation and defines the values of the diffusion coefficient and the pinch velocity in terms of quantities that can be determined from experiment. The deuterium diffusion coefficient can be determined from measured quantities—the ion-impurity collision frequency, which can be determined from the measured densities and temperatures, and the momentum transport frequency, which can be inferred from the measured toroidal rotation velocity. The unmeasured deuterium rotational velocity profile and the deuterium and carbon momentum transport frequencies were determined from the measured carbon toroidal rotation velocity by using first order perturbation theory.

A rather surprising feature was found in the measured toroidal rotation profile in the edge plasma. The measured carbon toroidal rotation velocity profile and the deuterium toroidal rotational velocity profile calculated from it were rather flat in L-mode, increased sharply within 30 ms of the L-H transition for $\rho < 0.95$, but decreased sharply during this same time interval for $\rho > 0.95$, indicating either a torque or an increased radial transport of toroidal momentum in the region $\rho > 0.95$ within the first 30 ms after the L-H transition. We have scrutinized the data and believe this reduction in toroidal rotation is real, for this discharge, but we have not yet determined if it is a universal feature of H-modes.

This increase in the interpreted momentum transport frequencies for $\rho > 0.95$ produced a sharp peaking in the interpreted deuterium diffusion coefficient immediately after the L-H transition. This structure for $\rho > 0.95$ gradually disappears from the measured rotation velocity and the interpreted diffusion coefficient profiles at later times. The overall effect is a transition from a diffusion coefficient profile in L-mode that increases sharply with radius for $\rho > 0.95$ to a fully developed H-mode diffusion coefficient profile in which the H-mode value is about twice the L-mode value for $\rho < 0.95$, but for $\rho > 0.95$ there is a pronounced reduction relative to L-mode and a "transport barrier" well-like structure of the diffusion coefficient caused by the structure in the experimental collision and momentum transport frequency profiles.

One possibility for the sharp reduction in co-current rotation for $\rho > 0.95$ within 30 ms after the L-H transition is ion orbit loss of preferentially counter-current ions, which was calculated to produce a co-current intrinsic rotation which increased with radius in the plasma edge. This intrinsic rotation was significant in L-mode, decreased significantly for $\rho > 0.95$ within the first 30 ms after the L-H transition, then increased with time after the first 30 ms. The magnitude of this change in intrinsic rotation was similar to the measured magnitude of the difference in toroidal rotation over the first 30 ms after the L-H transition.

The radial electric field, which was calculated from the radial momentum balance using measured carbon density, temperature, and rotation velocities, changed dramatically from the small, positive, and relatively flat L-mode profile to a profile which increased to positive values an order of magnitude larger (10-20 kV) for $\rho < 0.95$ but became strongly negative (-10 to 20 kV) for $\rho > 0.95$ immediately (within 30 ms) following the L-H transition. The electric field profile further evolved after 30 ms, non-monotonically but retaining these features, as the H-mode developed.

The pinch velocity is a collection of normalized electromagnetic forces, specified by momentum balance requirements, in which there are terms proportional to the toroidal and poloidal rotation velocities, a term proportional to the radial electric field, and (smaller) terms proportional to external momentum torques and the induced toroidal electric field. In this discharge, the radial electric field and the poloidal velocity terms were dominant. The variation in the radial electric field profile was the principle reason that the ion particle pinch velocity, which was only slightly inward ($\sim$10 m/s) for $\rho > 0.95$ in L-mode, became strongly inward ($\sim$100 m/s) in this region within 30 ms after the L-H transition and then remained strongly inward but of non-monotonically varying magnitude as the H-mode pedestal evolved. The deuterium poloidal rotation velocity (calculated from the deuterium radial momentum balance) also changed dramatically from the small, positive, and relatively flat L-mode profile to a H-mode profile strongly peaked (20-30 km/s) for $\rho > 0.95$.

The interpreted electron thermal diffusivity profile was relatively flat across the plasma edge in L-mode, but decreased sharply within 30–70 ms after the L-H transition to form a "transport barrier" structure and then varied, somewhat non-monotonically, as the H-mode pedestal fully developed. The interpreted ion thermal diffusivity profile was also relatively flat across the plasma edge in L-mode, and decreased sharply within 30-70 ms after the L-H transition, but did not discernibly form a "transport barrier" structure, and then further evolved, somewhat non-monotonically, as the H-mode pedestal fully developed. Calculation of ion-orbit loss effects in the edge plasma, which indicate steady increase in both particle and energy loss fractions as a function of time as the plasma enters the H-mode, were included in the ion heat diffusivity calculation.

Based on these results, we conclude that the majority of edge pedestal development occurs within the first 100 ms

following the L-H transition, for this discharge, and suggest that in future investigations it would be useful to obtain more highly time-resolved data over the first 50-100 ms after the L-H transition.

Finally, we note that the apparent spatio-temporal correlation among the calculated intrinsic rotation due to ion orbit loss, the measured torodial rotation and the measured radial electric field is suggestive that changes in ion orbit loss could be playing a major role in the dynamics of the pedestal buildup following the L-H transition, perhaps via the return edge current (necessary to compensate the ion orbit loss in order to maintain charge neutrality) setting the radial electric field in the plasma edge.

ACKNOWLEDGMENTS

This work was supported by the US Department of Energy under Grant No. DE-FG01-ER54538 with the Georgia Tech Research Corporation and Contract No. DE-AC03-99ER54463 with the General Atomics Company of Energy Cooperative Agreement No. DE-FC02-04ER54698.

APPENDIX: COMMENT ON POLOIDAL ROTATION

As noted in the body of the paper, there is some possible confusion in the literature about the direction and agreement with neoclassical theory of the poloidal rotation measurements. First, we note that a great deal of effort has been spent on refining the treatment of such things as the gyromotion effect[31] and making accurate measurements of the small Doppler shifts. Second, we note that different conventions (e.g., (i) the positive $\theta-$direction is upward at the outboard midplane, or (ii) the positive $\theta-$direction is taken in the theoretical right-hand sense in a right-hand $(r-\theta-\phi)$ coordinate system) have been used for reporting measured data. The second option is followed in this paper, with the positive toroidal direction taken in the counter-clockwise direction of the plasma current and the positive $\theta-$direction is taken in the right-hand sense, which is downward at the outboard midplane.

With regard to the question of the agreement of the measured poloidal rotation velocity with neoclassical theory, the main point to be made is that there are many different versions of poloidal rotation theory referred to in the literature as "neoclassical theory." Following the discussion of this subject in Ref. 32, the poloidal rotation is governed by the poloidal momentum balance, and the various versions of neoclassical theory depend on just which terms are retained in this equation and the theoretical evaluation of the viscous and friction terms. The best-known theory is the Hirshman-Sigmar theory,[33] which retains only the viscous and frictional terms and implicitly assumes poloidal symmetry of density and flows—a version of this H-S theory is in the NCLASS code.[34] A trace impurity approximation of the H-S theory yields the original Hazeltine[35] result of $V_{\theta i} \sim \partial T/\partial r$ for the main ions and the Kim-Diamond-Groebner (KDG) approximation[36] for the impurity ions. This KDG approximation and the results of the NCLASS calculation both are frequently referred to as neoclassical theory in experimental papers in which agreement or disagreement with neoclassical theory is claimed. There are other versions of neoclassical theory in which more terms are retained in the poloidal momentum balance and a different evaluation of the viscous term is used, and in which poloidal asymmetries in the density and flow are included, known as Stacey-Sigmar (S-S) theory.[32]

Although there have been mixed reports of agreement and disagreement between poloidal rotation measurements and various version of neoclassical theory, the most recent evidence indicates that when all the important terms are retained and poloidal asymmetries in density and flow are taken into account that the neoclassical prediction is in good agreement with experiment. An extended version of this S-S theory,[32] in which the poloidal asymmetries in the flux surface geometry were represented by the Miller model[37] and the poloidal asymmetries in density and flows were calculated, predicted the poloidal velocities measured in two DIII-D shots quite well.[38] Furthermore, recent measurements[39] of poloidal rotation in "matched" experiments in NSTX and DIII-D were found to be in reasonable agreement with each other and with a version of neoclassical theory.

[1]F. Wagner, G. Becker, K. Behringer, D. Campbell, A. Eberhagen, W. Engelhardt, G. Fussmann, O. Gehre, J. Gernhardt, G. V. Gierke, G. Haas, M. Huang, F. Karger, M. Keilhacker, O. Kluber, M. Kornherr, K. Lackner, G. Lisitano, G. G. Lister, H. M. Mayer, M. Meisel, E. R. Meuller, H. Murmann, N. Niedermeyer, W. Poschenrieder, H. Rapp, H. Rohr, F. Schneider, G. Siller, E. Speth, A. Staebler, K. H. Steuer, G. Venus, O. Vollmer, and Z. Yu, Phys. Rev. Lett. **49**, 1408 (1982).
[2]R. J. Groebner, K. H. Burrell, and R. P. Seraydarian, Phys. Rev. Lett. **64**, 3015 (1990).
[3]F. Wagner, Plasma Phys. Controlled Fusion **49**, B1 (2007).
[4]S. I. Itoh and K. Itoh, Phys. Rev. Lett. **60**, 2276 (1988).
[5]K. C. Shaing, E. C. Crume, and W. A. Houlberg, Phys. Fluids B **2**, 1492 (1990).
[6]K. H. Burrell, Phys. Plasmas **4**, 1499 (1997).
[7]P. W. Terry, Rev. Mod. Phys. **72**, 109 (2000).
[8]C. F. Maggi, Nucl. Fusion **50**, 066001 (2010).
[9]J. D. Callen, R. J. Groebner, T. H. Osborne, J. M. Canik, L. W. Owen. A. Y. Pankin, T. Rafiq, T. D. Rognlien, and W. M. Stacey, Nucl. Fusion **50**, 064004 (2010).
[10]W. M. Stacey, Phys. Plasmas **13**, 072510 (2006).
[11]W. M. Stacey, R. J. Groebner, and T. E. Evans, Nucl. Fusion **52**, 114020 (2012).
[12]W. M. Stacey, Fusion Sci. Technol. **63**, 34 (2013).
[13]J. Luxon, Nucl. Fusion **42**, 614 (2002).
[14]W. M. Stacey and R. J. Groebner, Phys. Plasmas **14**, 012501 (2007).
[15]W. M. Stacey and R. J. Groebner, Phys. Plasmas **17**, 112512 (2010).
[16]R. J. Groebner, T. H. Osborne, A. W. Leonard, and M. E. Fenstermacher, Nucl. Fusion **49**, 045013 (2009).
[17]T. N. Carlstrom, G. L. Campbell, J. C. DeBoo *et al.*, Rev. Sci. Instrum. **63**, 4901 (1992).
[18]P. Gohil, K. H. Burrell, R. J. Groebner *et al.*, in Proceedings of 14th Symposium Fusion Engineering, San Diego, 1991 (Institute of Electrical and Electronics Engineers, New York, 1992), Vol. 2, p. 1199.
[19]W. M. Stacey and R. J. Groebner, Nucl. Fusion **51**, 063024 (2011).
[20]T. H. Osborne, J. Phys. Conf. Series **123**, 012014 (2008).
[21]T. N. Carlstrom, K. H. Burrell, R. J. Groebner, A. W. Leonard, T. H. Osborne, and D. M. Thomas, Nucl. Fusion **39**, 1941 (1999).
[22]H. E. St. John, T. S. Taylor, Y.-R. Lin-Liu, and A. D. Turnbull, in *Proceedings of 15th IAEA Conference on Plasma Physics and Controlled Nuclear Fusion Research, Seville, 1994* (IAEA, Vienna, 1995), Vol. 3, p. 60.
[23]W. M. Stacey, Phys. Plasmas **5**, 1015 (1998); **8**, 3673 (2001); Nucl. Fusion **40**, 965 (2000).
[24]W. M. Stacey and R. J. Groebner, Phys. Plasmas **15**, 012503 (2008).
[25]B. A. Grierson, K. H. Burrell, W. M. Solomon, and N. A. Pablant, Rev. Sci. Instrum. **81**, 10D735 (2010).
[26]K. Miyamoto, Nucl. Fusion **36**, 927 (1996).

[27]W. M. Stacey, Phys. Plasmas **18**, 102504 (2011).
[28]J. S. deGrassie, R. J. Groebner, K. H. Burrell, and W. M. Solomon, Nucl. Fusion **49**, 085020 (2009).
[29]W. M. Stacey, J. A. Boedo, T. E. Evans, B. A. Grierson, and R. J. Groebner, Phys. Plasmas **19**, 112503 (2012).
[30]W. M. Stacey, Contrib. Plasma Phys. **48**(1–3), 94 (2008).
[31]W. M. Solomon and K. H. Burrell, Phys. Plasmas **13**, 056116 (2006).
[32]W. M. Stacey, Phys. Plasmas **15**, 012501 (2008).
[33]S. P. Hirshman and D. J. Sigmar, Nucl. Fusion **21**, 1079 (1981).
[34]W. A. Houlberg, K. C. Shaing, S. P. Hirshman, and M. C. Zarnstorff, Phys. Plasmas **4**, 3230 (1997).
[35]R. D. Hazeltine, Phys. Fluids **17**, 961 (1974).
[36]B. Kim, P. H. Diamond, and R. J. Groebner, Phys. Fluids B **3**, 2050 (1991).
[37]R. L. Miller, M. S. Chu, J. M. Greene, and Y. R. Lin-Liu, Phys. Plasmas **5**, 973 (1998).
[38]C. Bae, W. M. Stacey, and W. M. Solomon, "Extension of neoclassical rotation theory for tokamaks to realistically account for the geometry of magnetic flux surfaces," Nucl. Fusion (submitted).
[39]K. H. Burrell, E. A. Belli, W. M. Solomon, B. A. Grierson, W. Wang, and G. W. Rewoldt, "Impurity poloidal rotation in DIII-D under low toroidal field conditions," Bull. Am. Phys. Soc. **55**, GP9.56 (2010).